https://doi.org/10.5194/essd-2025-281
Preprint. Discussion started: 30 May 2025

Open Access Earth System Science Data Discussions

A decadal, hourly high-resolution satellite dataset of aerosol optical properties over East Asia

Jeewoo Lee[1], Jhoon Kim[1], Seoyoung Lee[2,3], Myungje Choi[2,3], Jaehwa Lee[3,4], Daniel J. Jacob[5], Su Keun Kuk[6], Young-Je Park[7]

[1]Department of Atmospheric Sciences, Yonsei University, Seoul, Republic of Korea
[2]Goddard Earth Sciences Technology and Research II, University of Maryland Baltimore County, Baltimore, MD, United States
[3]NASA Goddard Space Flight Center, Greenbelt, MD, United States
[4]Earth System Science Interdisciplinary Center, University of Maryland, College Park, MD, United States
[5]School of Engineering and Applied Sciences, Harvard University, Cambridge, United States
[6]Samsung Particulate Matter Research Institute, Samsung Advanced Institute of Technology, Gyeonggi-do, Republic of Korea
[7]TelePIX Co., Ltd., Seoul, Republic of Korea

Correspondence to: Jhoon Kim (jkim2@yonsei.ac.kr)

Abstract. Formerly known as one of the most polluted regions of the globe, East Asia underwent a dramatic improvement of air quality, especially for aerosols, starting in the 2010s. Numerous satellites have observed East Asia for a long time duration, but often with a low spatial or temporal resolution, limiting their ability to capture small-scale variabilities or provide continuous observations of long-range transport of aerosols. In this study, we provide an hourly aerosol optical property (AOP) dataset retrieved from the Korean Geostationary Ocean Color Imager (GOCI), with a high spatial resolution of 2 km at nadir, covering the entire operational period from March 2011–March 2021. The dataset is retrieved using the Yonsei Aerosol Retrieval Algorithm, providing aerosol optical depth (AOD) at 550 nm as the primary product, along with fine mode fraction, single scattering albedo, Ångström exponent, and aerosol type as ancillary products. Seasonal validation of AOD against the Aerosol Robotic Network (AERONET) showed that the fraction of data points within the expected error range of 0.05 + 15% varied from 56.4% in June-July-August to 64.5% in September-October-December, with the mean bias generally within ±0.05. Compared to the operational version, the high-resolution product demonstrated improved retrieval capability in the presence of broken clouds, along complex coastlines, and in capturing AOD variability at the sub-district level. The decadal AOD exhibited a decreasing trend over four major cities within the observation domain. We expect this data to be widely used in climate modelling, reanalysis, atmospheric chemistry, marine optics, environmental health studies, variability and trend analysis, contributing to a more comprehensive understanding of the interactions between climate change, trace gases, human health, and AOPs. The dataset presented in this work is publicly available for download at https://doi.org/10.7910/DVN/WWLI4W (Lee et al., 2025).

https://doi.org/10.5194/essd-2025-281
Preprint. Discussion started: 30 May 2025

1 Introduction

Atmospheric aerosols play an important role in air pollution and climate change. The presence of ambient aerosols reduces visibility, and the exposure deteriorates human health by increasing the mortality rate and the probability of cardiovascular diseases, asthma, and neurodegenerative diseases (Charlson, 1969; Dockery et al., 1992; Baldacci et al., 2015; Wang et al., 2017; Pye et al., 2021). In addition, aerosols can act as a medium for atmospheric chemical reactions, influencing the concentration of atmospheric trace gases (Andreae and Crutzen, 1997). Importantly, aerosols are one of the major components that offset the warming effect of greenhouse gases by scattering solar radiation, exerting a net cooling effect (Kaufman et al., 2002; Bellouin et al., 2020; IPCC, 2021). From 1750 to 2019, the effective radiative forcing of atmospheric aerosols in total is estimated to be -1.1 W m^{-2}, compared to +2.16 W m^{-2} for carbon dioxide (IPCC, 2021). Thus, long-term data of aerosol optical properties (AOPs) can serve as a fundamental resource for research across various fields.

There have been extensive studies on the effects and distribution of aerosols especially over East Asia, as the region is renowned for massive emissions of aerosols and their precursors. To this end, air quality campaigns such as the Distributed Regional Aerosol Gridded Observation Networks – Northeast (DRAGON-NE) Asia 2012 campaign and the Korea–United States Air Quality (KORUS-AQ) field study that leveraged airplanes and surface sites equipped with various in-situ and remote sensing measurement instruments were conducted to investigate the atmospheric environment over Northeast Asia (Holben et al., 2018; Crawford et al., 2021). According to the World Health Organization (WHO), South and East Asia are the most polluted regions in terms of surface-level particulate matter (PM), showing the highest annual population-weighted particulate matter smaller than 2.5 μm in diameter ($PM_{2.5}$) in 2019 (WHO, 2021). This poses a major threat over East Asia, compared to Europe, North America, and the Western Pacific, where the exposure to particulates is decreasing. While approximately 0.2 million excess deaths were estimated in the United States and Canada due to aerosol exposure, China, India, and other parts of Asia were expected to experience 2.4 million, 2.2 million, 1.3 million excess deaths, respectively, due to high aerosol concentration (Burnett et al., 2018). As a result, East Asian countries have implemented policies aimed at managing air quality. For instance, China implemented the Clean Air Action in 2013, which resulted in a steep reduction of anthropogenic air pollutants, including aerosols and their precursors (Zheng et al., 2018). Similarly, South Korea has consistently adopted air quality improvement plans for its capital city, the Seoul Metropolitan Area (SMA), since 2005 (Korea Ministry of Environment or KMOE, 2005; KMOE, 2013). SMA achieved an 8% and 10% reduction in mortality rates from cardiovascular and cerebrovascular diseases through PM reduction in 2012–2013 compared to 2004–2005 (Han et al., 2018). Air quality concerns are not confined to individual countries but rather represent a cross-boundary challenge. In addition, strong westerlies over Northeastern Asia facilitate long-range transport of aerosols, adding complexity to studies on aerosol distribution (Lee et al., 2019; Lee et al., 2021).

Satellite observations provide spatially continuous data unlike in-situ measurements. Primarily, they provide the amount of atmospheric aerosols as aerosol optical depth (AOD), a measure of aerosol extinction within a vertical column of air from the Earth's surface to the top-of atmosphere (TOA). For example, the Moderate Resolution Imaging Spectroradiometer (MODIS)

https://doi.org/10.5194/essd-2025-281
Preprint. Discussion started: 30 May 2025

onboard Terra and Aqua views the sunlit side of the entire globe every one or two days. MODIS AOD products, such as Dark Target (DT), Deep Blue (DB), and Multi-Angle Implementation of Atmospheric Correction (MAIAC), have demonstrated strong agreement with ground-based observations such as the Aerosol Robotic Network (AERONET) (Levy et al., 2010; Hsu et al., 2013; Levy et al., 2013; Lyapustin et al., 2018; Hsu et al., 2019). To continue the long-term AOD records, these algorithms have been implemented on other satellites, such as the Visible Infrared Imaging Radiometer Suite (VIIRS) (Hsu et al., 2019; Sawyer et al., 2020; Lee et al., 2024) with cross-calibration to MODIS (Lyapustin et al., 2023). However, because of the coarse temporal resolution, these low Earth orbit (LEO) satellites are less effective for studying diurnal variations and instantaneous peaks of observables (International Ocean-Colour Coordinating Group (IOCCG), 2012; Kim et al., 2020). In contrast, Geostationary Earth Orbit (GEO) satellites observe a certain domain with a high spatial and temporal resolution. For instance, the Geostationary Ocean Color Imager (GOCI) onboard the Communication, Ocean and Meteorological Satellite (COMS, also known as GK-1), the first ocean color imager in GEO was launched in 2010 and observed East Asia for 10 years. It observed East Asia eight times hourly during daytime, from 00 UTC to 07 UTC, with a spatial resolution of 500 m × 500 m at nadir. GOCI was equipped with six visible and two near-infrared (NIR) bands, ranging from 412 nm to 865 nm. This multispectral information provides advantages for aerosol retrieval compared to the conventional 5-channel Meteorological Imager (MI) on the same platform with only one visible channel, offering relatively limited information content for aerosol retrieval (Kim et al., 2016). The operational algorithm for GOCI aerosol retrieval, the Yonsei Aerosol Retrieval Algorithm (YAER), provided hourly AOD over cloud-free and snow/ice-free pixels with a 6 km × 6 km resolution for data quality assurance (Lee et al., 2010a; Choi et al., 2016; Choi et al., 2018).

The GOCI YAER product has been widely used in aerosol studies, contributing not only to regional analyses over East Asia but also to a deeper understanding of aerosols in general. For instance, surface-level $PM_{2.5}$ concentration was estimated through the integration of chemical transport models or data assimilation in East Asia (Saide et al., 2014; Xu et al., 2015; Pang et al., 2018; Pendergrass et al., 2025). The products also played a crucial role in unravelling the aerosol properties during the DRAGON-NE Asia and the KORUS-AQ campaigns (Choi et al., 2016; Lennartson et al., 2018; Choi et al., 2019; Lim et al., 2021).

To continue the GOCI mission, GOCI-II was launched in February 2020. Driven by improved sensor technology, GOCI-II now features a higher spatial resolution of 250 m × 250 m at nadir, effectively meeting the evolving needs of present-day users. According to Lee et al. (2023), the higher resolution of the GOCI-II YAER product has increased the amount of AOD data by a factor of five compared to the GOCI YAER operational product, enabling more detailed atmospheric monitoring. Building upon these technological advancements, some studies have pointed out the need for higher spatiotemporal resolutions of satellite products for air quality assessments (Lee et al., 2024). Other GEO missions such as the Advanced Meteorological Imager and the Geostationary Environment Monitoring Spectrometer were also launched in the same era of GOCI-II to monitor the atmosphere of East Asia (Kim et al., 2020; Kim et al., 2024). Over these state-of-the-art satellites, GOCI has a relative advantage on its diverse spectral bands in the visible spectrum, its long-term observation records with stability, and the presence of a successor satellite to continue its mission. Furthermore, it meets the sustained demand for high-resolution AOP

https://doi.org/10.5194/essd-2025-281
Preprint. Discussion started: 30 May 2025

datasets over the long term in air quality research and related applications, including aerosol-cloud interaction and epidemiological studies (e.g. Eck et al., 2020; Pu and Yoo, 2022).

Here, we present a high-resolution, decadal hourly AOPs dataset over East Asia based on GOCI YAER, which is challenging with respect to data quality due to limited number of pixels available. The spatial resolution of the product has been increased ninefold (2 km × 2 km) compared to the operational version (6 km × 6 km). Validation against AERONET, analysis of diurnal variation, and cases studies highlighting the strengths of high-resolution data are provided. The dataset and high-resolution YAER algorithm are described in Section 2. Section 3 presents the characteristics of the AOPs, validation results and analysis of the data record. The availability of data is presented in Section 4. Section 5 summarizes and concludes the study.

2 Materials and methodology

2.1 Retrieval algorithm

The GOCI high-resolution YAER goes through three main steps to retrieve the hourly AOPs dataset. The inputs used for retrieval are listed in Table 1.

Table 1. List of input data for GOCI high-resolution YAER.

Input data	Usage
GOCI Level 1B	Step 1: TOA reflectance calculation
ECMWF ERA 5 wind speed climatology	Step 3: inversion over ocean
Land surface reflectance climatology	Step 3: inversion over land and turbid water
Global Multi-resolution Terrain Elevation Data (GMTED)	Step 3: inversion over land, ocean, and turbid water
Ocean LUT	Step 3: inversion over ocean
Land LUT	Step 3: inversion over land and turbid water

2.1.1 Step 1: Cloud detection and pixel aggregation

The cloud detection for the high-resolution GOCI dataset is the same as used for the operational dataset, as described in Choi et al. (2018). A brief description is provided here. The algorithm reads hourly GOCI observed radiances of wavelengths centered at 412, 443, 490, 555, 660, 680, 745, and 865 nm along with geolocation and observation geometry information. These values have a spatial resolution of 500 m × 500 m at nadir (‘observation resolution’). Then, the TOA reflectance of each wavelength can be calculated using eq. (1):

$$\rho_\lambda = \frac{\pi \cdot L_\lambda}{\mu_0 \cdot E_\lambda}, \quad (1)$$

https://doi.org/10.5194/essd-2025-281
Preprint. Discussion started: 30 May 2025

Open Access Earth System Science Data Discussions

where λ is the GOCI wavelength, μ_0 is the cosine of solar zenith angle, L_λ is the observed radiance from GOCI, and E_λ is the solar extraterrestrial flux.

In this step, the spectral TOA reflectance is used to detect and remove pixels that are inappropriate for aerosol retrieval, such as clouds, snow, and bright surfaces, which cannot be distinguished from aerosol signals in most situations in the visible spectra. Clouds are bright in visible wavelengths, and cloud edges and broken clouds are spatially inhomogeneous compared to clear-sky pixels. Considering these physical and optical properties of clouds, clouds over land and ocean are detected separately. For clouds over ocean, a TOA reflectance threshold test and a 3 × 3 pixel standard deviation test are applied. For clouds over land, the detection includes a TOA reflectance threshold test, reflectance ratio test, the 3 × 3 pixel standard deviation and mean test, and the normalized difference vegetation index (NDVI) test for inland water detection. In addition, pixels affected by sun glints over water are removed. After the cloud detection, dusty pixels and heavy aerosols initially misclassified as clouds are reinstated based on TOA reflectance ratios and 3 × 3 pixel standard deviation and mean.

The remaining clear-sky pixels are converted into 2 km × 2 km resolution ('product resolution') for aerosol retrieval by aggregating 4 × 4 observation pixels. When collecting the clear-sky pixels within the 4 × 4 box, the brightest 60% and the darkest 20% of pixels within the box are excluded from averaging to minimize residual cloud effects or cloud shadows. Additional cloud detection and bright surface removal is conducted at the product resolution. Ancillary variables needed for retrieval, such as longitude, latitude, land-sea mask, geometry, are averaged and aggregated into the product resolution without screening.

2.1.2 Step 2: Classification of surface regimes

To allocate the clear-sky product resolution pixels into their corresponding surface regimes, the land-sea mask is used to discriminate land and ocean pixels. The ocean pixels are further divided into turbid water and the open ocean (hereafter ocean) using the $\Delta\rho_{660}$. The $\Delta\rho_{660}$ is the difference between TOA reflectance at 660 nm and the interpolated value between 412 nm and 865 nm at 660 nm (Li et al., 2003; Choi et al., 2016). Ocean pixels with $\Delta\rho_{660}$ between -0.05 and -0.01, and high TOA reflectance at 660 nm are classified as turbid water and are put into the turbid water algorithm.

For both the land and turbid water algorithms, the surface reflectance is calculated based on the minimum reflectance technique (Koelemeijer et al., 2003; Hsu et al., 2004). We calculated the Rayleigh-corrected reflectance (RCR) for every GOCI observations at the observation resolution ranging from March 2011 to February 2016. The minimum reflectance technique assumes that there would be at least a single cloud-free, aerosol-free scene within the sampling period, which can be represented by the darkest values of RCR. Here, we averaged the darkest 1–3% of RCR for each month and wavelength as the *a priori* of GOCI monthly surface reflectance.

The ocean algorithm adopts the Cox and Munk method, where the wind speed of the water surface is used to calculate the surface reflectance (Cox and Munk, 1954). We collected the wind speed at 10 m above sea level from the European Centre for Medium-Range Weather Forecasts Interim dataset. The dataset has 0.25° × 0.25° resolution, and a 5-year average of each

https://doi.org/10.5194/essd-2025-281
Preprint. Discussion started: 30 May 2025

month was taken as the *a priori*. For both land and ocean, the *a priori* are set to the value for the 15th day of each month, and the values for other days are calculated by linearly interpolating the *a priori* of two adjacent months.

2.1.3 Step 3: Inversion

The GOCI high-resolution YAER utilizes the LUT to efficiently retrieve AOD from vast number of pixels. Two LUTs, the land LUT and ocean LUT, are constructed using libRadtran radiative transfer package (Mayer and Kylling, 2005). The land LUT is composed of wavelength, solar zenith angle (SZA), satellite viewing zenith angle (VZA), relative azimuth angle (RAA), AOD, surface reflectance, surface altitude, and aerosol type nodes, and that of ocean is composed of wavelength, SZA, VZA, RAA, AOD, wind speed, and aerosol type. The aerosol models are derived from AERONET AOP climatology prior to the GOCI observation period. The AOD nodes within the LUT range from 0 to 3.6, and negative AOD values due to extrapolation are permitted down to -0.05. 26 aerosol models were assumed, which are classified into three absorbing criteria and nine size criteria according to SSA and FMF, respectively.

During the inversion process, different wavelengths are used for different surface regimes. For land, wavelengths 412 to 680 nm are used for inversion, and only pixels with surface reflectance lower than 0.15 at these selected wavelengths are used in the inversion process. For ocean and turbid water, wavelengths 412, 443, 745, and 865 nm, and 412 and 865 nm are selected, respectively, to avoid channels with high water-leaving radiance (Ahn et al., 2012). For all surface regimes, only pixels with SZA smaller than 70° are used. The algorithm selects three aerosol models that have the lowest standard deviation of 550 nm AODs retrieved from individual spectral bands. Then, the spectrally averaged 550 nm AODs for each of these three models are used to calculate the final AOD, which is determined as a weighted mean of the averaged AODs, with weights based on the inverse of the standard deviation. FMF, SSA, AE are determined based on the selected aerosol models and their corresponding weights. The aerosol type is then classified into six types from FMF and SSA thresholds: dust, non-absorbing coarse, mixture, highly-absorbing fine, moderately-absorbing fine, and non-absorbing fine (Lee et al., 2010b).

2.2 Dataset description

The GOCI high-resolution AOPs are provided for clear-sky pixels over land, ocean, and turbid water. The field of regard (FOR) of GOCI is shown in Fig. 1. The wedge pattern on the left and right edges of Fig 1 results from the 16 slots comprising the observation (Ryu et al., 2012). In the retrieval process and the resulting dataset, all slots are merged into a single scene for the user's convenience. The dataset ranges from March 1st, 00:30 UTC, 2011 to March 31st, 07:30 UTC, 2021. The proposed GOCI YAER high-resolution AOPs dataset consists of five properties: AOD at 550 nm, single scattering albedo (SSA) at 440 nm, fine mode fraction (FMF) at 550 nm, Ångström exponent (AE) between 440 nm and 870 nm, and aerosol type. Unless otherwise stated, the AOD, FMF, SSA, and AE of in this study are at the wavelength of GOCI YAER. The AOD is retrieved by comparing measured and calculated TOA reflectance, and the other four variables are derived from selected aerosol models for AOD retrieval. The SSA quantifies the measure of aerosol scattering properties, defined as the ratio of aerosol scattering to extinction. FMF and AE are the measure of aerosol size, which can act as a proxy for anthropogenic aerosols (Anderson et

https://doi.org/10.5194/essd-2025-281
Preprint. Discussion started: 30 May 2025

al., 2005). Aerosol type is determined from the SSA and FMF, following the work of Lee et al. (2010b). Since FMF, SSA, AE, and aerosol type are ancillary variables, it is recommended that these variables be used qualitatively or for interpreting the AOD error. The notation of the variables within the dataset and their respective dimensions are listed in Table 2.

Due to the large file size, the dataset is saved in zipped files in tar.gz format, on a monthly basis. The zipped files are named following the "*GOCI_YAERAERO_hires_{YYYYMoMo}.tar.gz*" convention, where *YYYY* and *MoMo* are 4-digit numeric year and 2-digit month, respectively. The zipped files include hourly dataset in NetCDF-4 format, and the file names are structured following the "*GOCI_YAERAERO_hires_{YYYYMoMoDDHHMiMiSS}.nc*" convention, where *DD*, *HH*, *MiMi*, *SS* indicate the 2-digit numeric day, hour, minute, and seconds of GOCI observation time.

Table 2. List of variables in the GOCI high-resolution AOPs product.

Variable name	Long description	dimensions
Aerosol_Optical_Depth	Aerosol Optical Depth at 550 nm	2D; (latitude=1421, longitude=1391)
Aerosol_Type	Aerosol type: 1 = Dust, 2 = Non-absorbing Coarse, 3 = Mixture, 4 = High-absorbing Fine, 5 = Moderate-absorbing Fine, 6 = Non-absorbing Fine	2D; (latitude=1421, longitude=1391)
Angstrom_Exponent	Calculated Angstrom Exponent between 440 and 870 nm	2D; (latitude=1421, longitude=1391)
Fine_Mode_Fraction	Fine Mode Fraction at 550 nm	2D; (latitude=1421, longitude=1391)
Single_Scattering_Albedo	Single Scattering Albedo at 440 nm	2D; (latitude=1421, longitude=1391)

https://doi.org/10.5194/essd-2025-281
Preprint. Discussion started: 30 May 2025

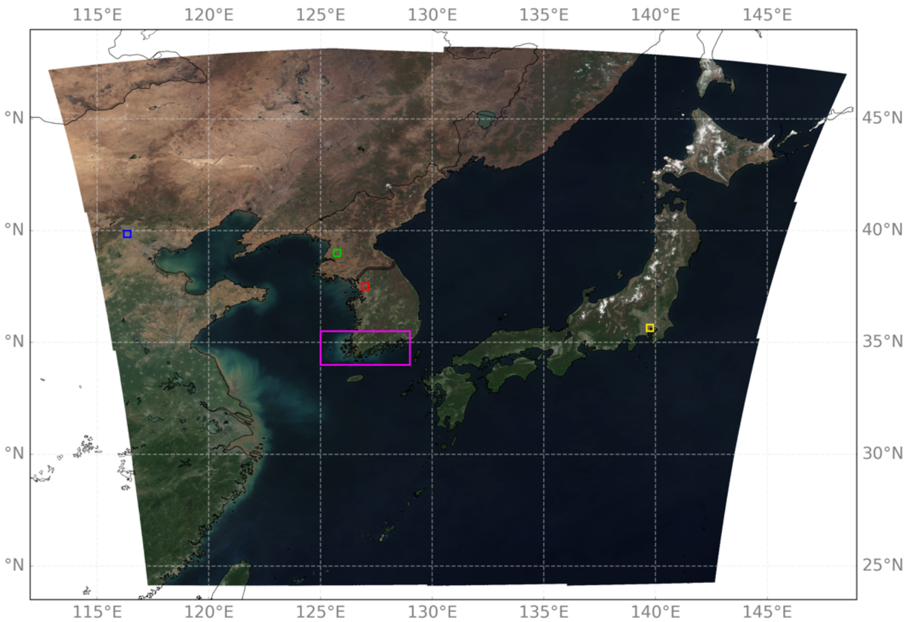

Figure 1. The field of regard of GOCI. The background represents the RGB composite of surface reflectance database of April, 03 UTC. The blue, green, red, yellow boxes indicate the location of 0.3˚ × 0.3˚ grid encompassing the four major cities within the GOCI domain, Beijing, Pyongyang, Seoul, and Tokyo, respectively. The magenta box indicates the southwestern coast of the Korean Peninsula shown in Fig. 3.

3 Results and discussion

3.1 Data characteristics

The characteristics and strengths of GOCI high-resolution AOD are presented in this section. Figure 2 shows an example of GOCI high-resolution and operational AOD over two cloudy scenes in the Pacific Ocean. Amongst the complex cloud structures, the AOD is retrieved over cloud-free pixels that pass the cloud masking algorithm. Compared to the operational AOD products (Fig. 2b and e), the fine-scale AOD between cloud structures is more pronounced in the high-resolution AOD (Fig. 2a and d). The larger pixel size of the operational product (Fig. 2b and e) may make the retrieved area appear more extensive. However, this implies that the observation resolution pixels are incorporated to represent an area that encompasses farther locations during the 6 km aggregation process. Over a horizontal plane, the number of high-resolution pixels within the domain was more than double that of the operational version (Fig. 2c and f). In addition, the 2 km pixels are in close proximity of cloud pixels, providing a more precise information on AOD over cloud-free areas which are surrounded by clouds.

https://doi.org/10.5194/essd-2025-281
Preprint. Discussion started: 30 May 2025

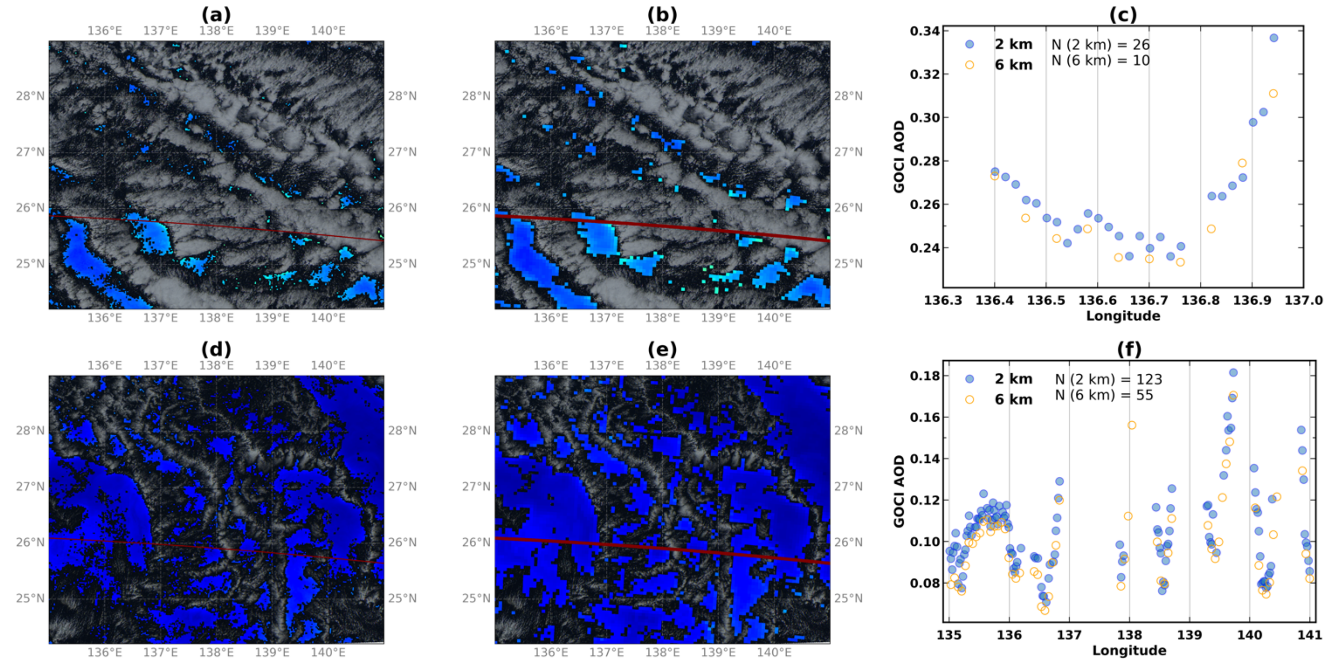

Figure 2. GOCI AOD on January 27th, 2018, 02 UTC (top panel) and March 11st, 2018, 00 UTC (bottom panel) over the Pacific Ocean. GOCI high-resolution AOD (a, d), the operational AOD (b, e) and the comparison of two data over a horizontal plane (c, f) are shown. Red lines over the four maps (a, b, c, d) indicate the longitudinal pixels used for constructing (c) and (f).

Figure 3 shows two cases over the southwestern coast of the Korean Peninsula, which is characterized by a complex coastline with countless small islands and bays, and frequent occurrences of turbid water. Studies on GOCI ocean color algorithms such as atmospheric correction, algae blooms, chlorophyll-a, and turbidity have focused on these regions (Ahn et al., 2012; Choi et al., 2012; Choi et al., 2014; Kim et al., 2016; Lee et al., 2021). Here, AOD information is critical for atmospheric correction, which is fundamental for earning oceanic optical properties. Therefore, we investigated the potential of high-resolution AOD products over complex coastlines and their comparative advantage over operational products.

Two characteristics stand out over the domain. First, the operational version of AOD of Fig. 3 shows a discrete, artifactual boundary over pixels with mixed terrain of island and open ocean. This is because a single coarse 6 km pixel over coastal areas reflects the combined signals from both island and ocean simultaneously. On the other hand, the high-resolution AOD pixels over small islands and the surrounding ocean are distinctly delineated, providing reliable information for both regimes. Second, the extent of turbid water pixels appearing as high AOD has decreased, due to a finer scale of land-sea mask resolution and fewer pixels used in aggregation. Because the coastlines are complicated, the turbidity of water over this region is spatially highly variable; in the operational version, since a larger number of pixels are aggregated to constitute a retrieval pixel, some coastal pixels are misrepresented. Comparatively, the high-resolution AOD displays a finer variation of AOD (Fig. 3a) and a more realistic view of AOD over turbid water (Fig. 3b). Overall, these characteristics of high-resolution products are expected to be valuable for other research fields such as marine optics and oceanography as well.

https://doi.org/10.5194/essd-2025-281
Preprint. Discussion started: 30 May 2025

Open Access Earth System Science Data Discussions

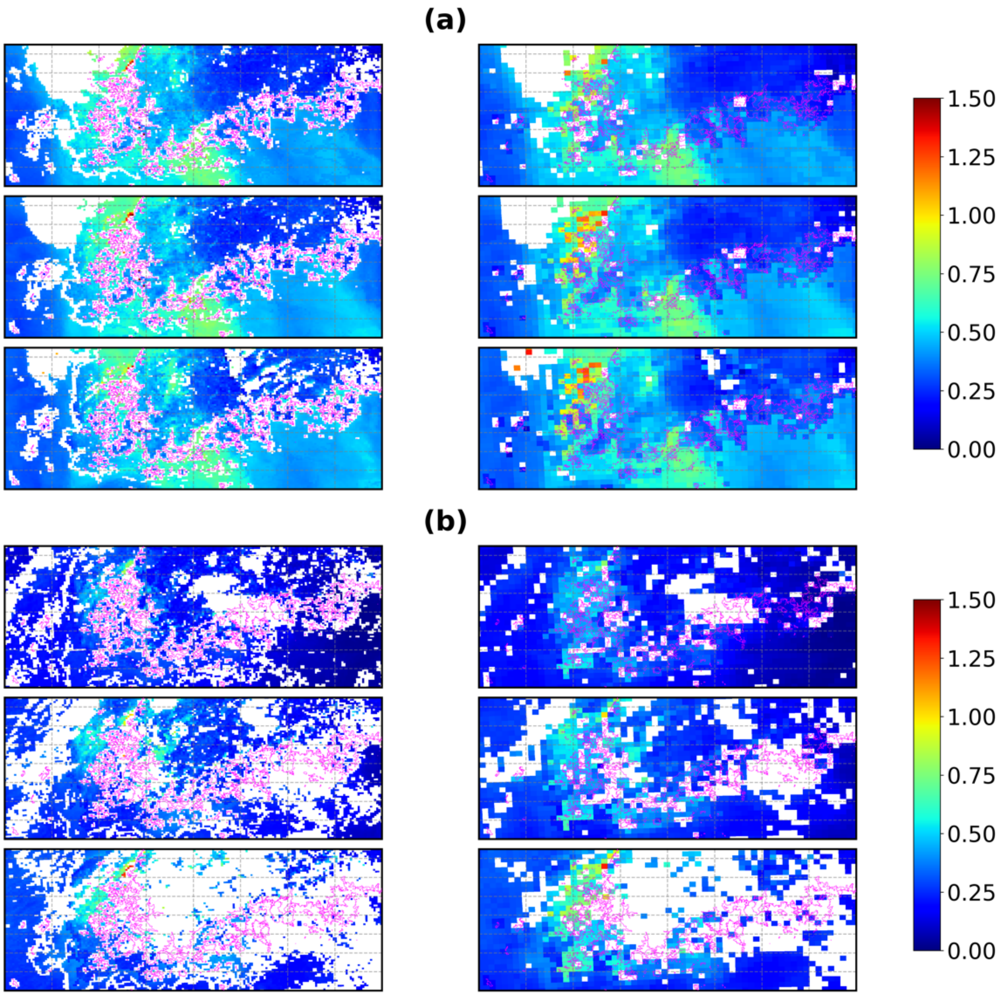

Figure 3. GOCI high-resolution AOD (left panel) and operational AOD (right panel) over the southwestern coast of the Korean Peninsula (magenta box, Fig. 1) for (a) May 14th, 2018, and (b) October 28th, 2018, respectively. Each set of three maps show the AOD of 00–02 UTC (top to bottom). Pink lines indicate the coastlines.

The competence of the high-resolution product is further examined for a highly populated megacity, namely the SMA of South Korea. Approximately half of the country's population reside in SMA, setting a large number of residents vulnerable to local air pollution (https://www.index.go.kr). Figure 4 shows an incident of medium- to high AOD case on May 9th, 2012, amid the DRAGON-NE campaign. As extra AERONET sites were set up during the campaign, maximum of 10 sites including the sites with long-term records are shown. The unique feature of the high-resolution product is the masked pixels across the figures, which are due to the presence of the Han River. The respective 6 km pixels including the Han River were not screened out because although the inland water pixels in the observation resolution were masked out successfully, the adjacent land pixels within the same 6 km pixel met the aggregation criteria. Therefore, it can be inferred that the 2 km products effectively eliminate the influence of inappropriate pixels in fine geographical features.

https://doi.org/10.5194/essd-2025-281
Preprint. Discussion started: 30 May 2025

The AOD distributions of 2 km products (left panel of Fig. 4) and the 6 km products (right panel of Fig. 4) are similar, but more subtle features are depicted in the high-resolution products. The high-resolution pixels located within the corresponding 6 km pixel are not a simple super-resolution version of the 6 km version but effectively represents the sub-pixel variability within the 6 km pixel. Furthermore, while a single pixel of the 6 km product covers one or more sub-districts of SMA, multiple high-resolution 2 km pixels fall into a single sub-district, providing more specific information both socially and geographically.

https://doi.org/10.5194/essd-2025-281
Preprint. Discussion started: 30 May 2025

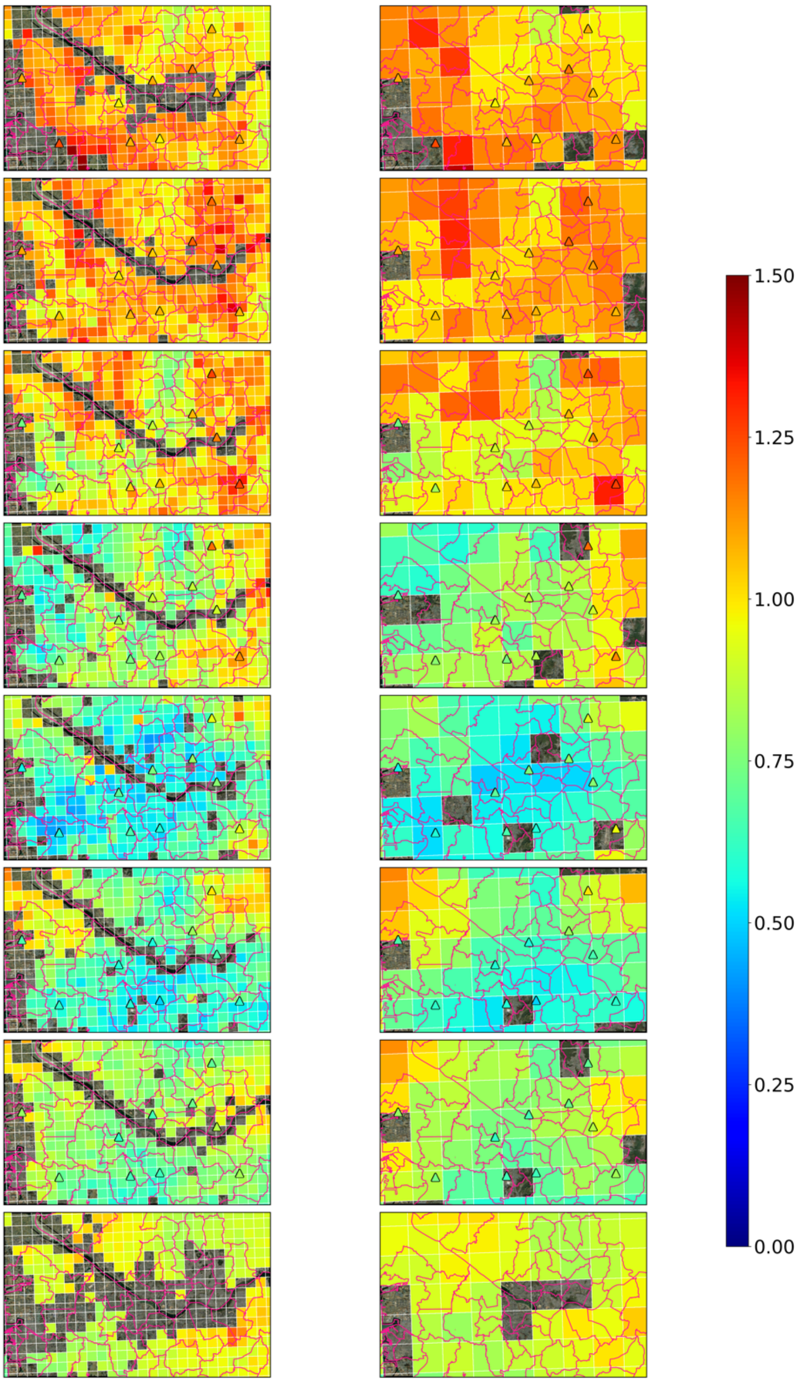

Figure 4. GOCI high-resolution AOD (left panel) and operational AOD (right panel) for May 9th, 2012, over the SMA (37.4–37.7˚N, 126.6–127.2˚E). The red lines on the map indicate the sub-districts of SMA, and the triangles and the filled colors represents AERONET locations and their respective collocated AOD.

https://doi.org/10.5194/essd-2025-281
Preprint. Discussion started: 30 May 2025

3.2 Validation

We validated the GOCI high-resolution YAER AOD to AERONET AOD, which is widely employed as ground truth for satellite AOPs validation owing to its low uncertainties (Holben et al., 1998). In the visible spectra, the uncertainty of AERONET AOD is known to be around 0.01, which is much lower than that of satellites (Eck et al., 1999). Here, we used the AERONET Version 3 Level 2.0 direct sun AOD for validation, and the AOD at 550 nm was obtained by a quadratic interpolation of spectral AERONET AOD (Giles et al., 2019; Sinyuk et al., 2020). For collocation of GOCI high-resolution YAER products and AERONET, AERONET observations within the ±30 minutes from GOCI observation time and the retrieved pixels within the 25 km radius around each AERONET site were averaged, respectively. AERONET sites for short-term temporary usage were excluded, leaving 39 sites for analysis. The expected error (EE) envelope is defined as EE = ± (0.15 × AERONET AOD + 0.05), following the MODIS DT standards of Levy et al. (2013). Figure 5 shows the validation results of the whole GOCI observation period, divided into four seasons. For all four seasons, 56-66% of the collocated retrievals are within the EE envelope, indicating a reasonable accuracy compared to AERONET. Collocated points were most abundant during spring (Fig. 5b, March–May, MAM), which can be attributed to two causes; lower SZA and a reduced portion of clouds and snowy surfaces leading to an increase in retrieved GOCI pixels; additional AERONET sites were set up to support the DRAGON-NE campaign in spring 2012. The portion of GOCI and AERONET AOD >1.5 was 0.02%, 0.93%, 2.8%, and 0.85% for winter, spring, summer, and autumn, respectively. The higher portion of high AOD in summer is due to aerosol hygroscopic growth, driven by the high relative humidity over East Asia during this season (Zhai et al., 2021). Validation results divided into land and ocean are shown in Fig. A1 and A2, respectively. The validation criteria are the same for Fig. 5, but ocean and land pixels were masked when validating for land and ocean, respectively. Validation for ocean had better results, because there are fewer uncertainties arising from surface reflectance over open ocean.

Figure 6 shows the fraction of GOCI AOD retrievals within the expected error and the Pearson correlation coefficient compared to AERONET measurements at individual sites. Although there were some variations, most sites showed a R > 0.8, % within EE > 60% and MBE < 0.05, indicating that there is no significant bias according to geographical location. The median value of site-wise validation was 60% and 0.82 for % within EE and R, respectively.

https://doi.org/10.5194/essd-2025-281
Preprint. Discussion started: 30 May 2025

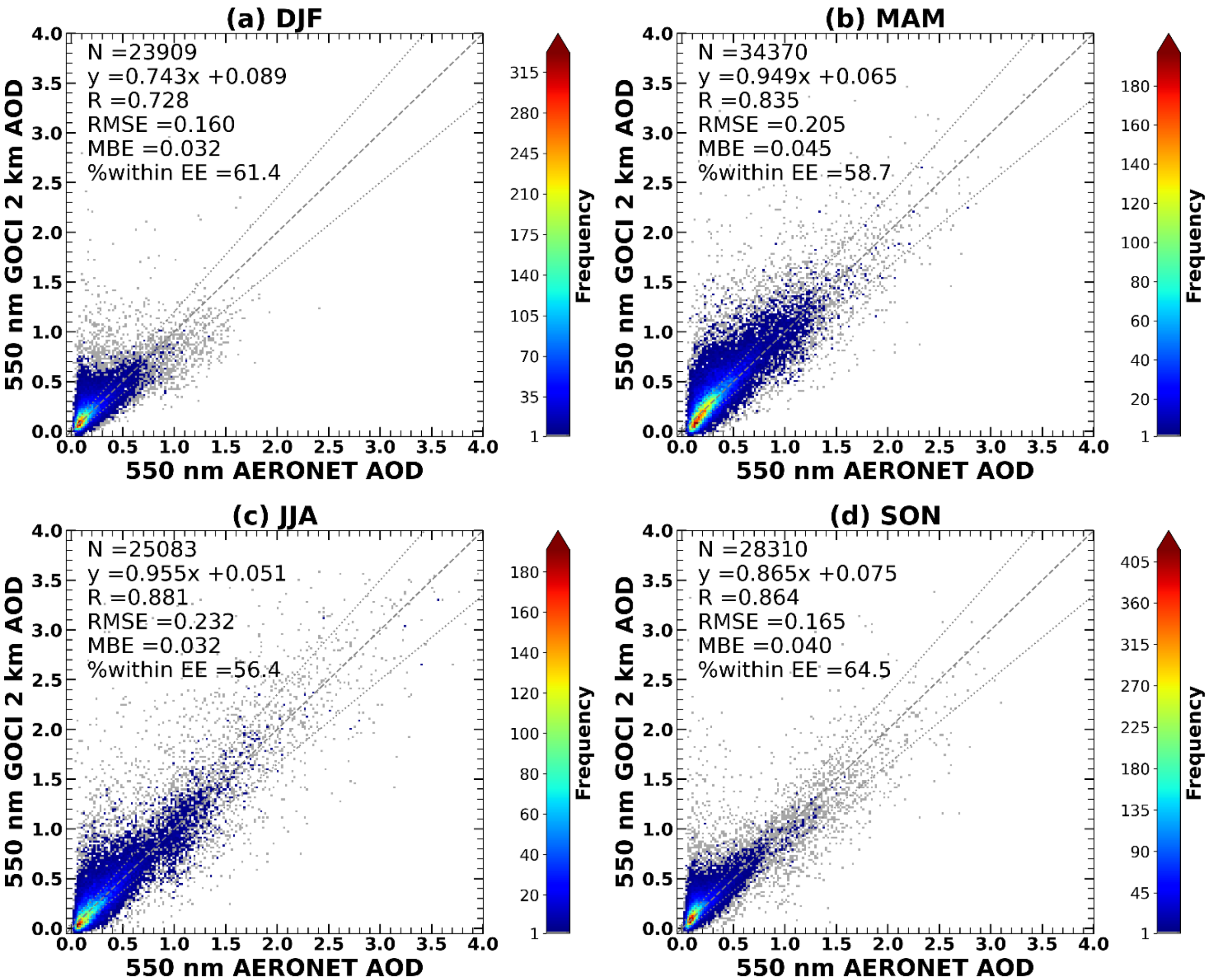

Figure 5. Validation of GOCI high-resolution YAER AOD to AERONET AOD during the whole observation period, classified into four seasons: (a) winter, (b) spring, (c) summer, and (d) autumn. The number of collocated points (N), correlation coefficients (R), the root mean squared error (RMSE), and mean bias error (MBE) are shown for each plot.

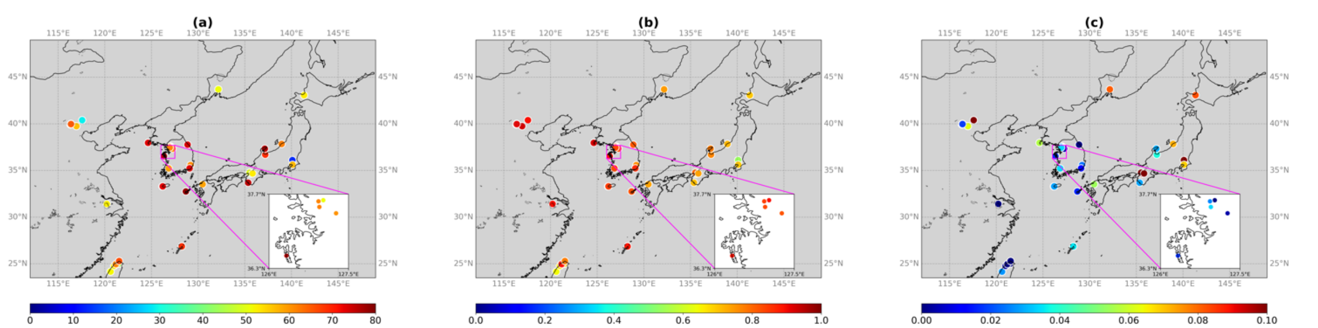

https://doi.org/10.5194/essd-2025-281
Preprint. Discussion started: 30 May 2025

Figure 6. Validation metrics for AERONET sites within the GOCI domain, for (a) the % within EE envelope, (b) R, (c) MBE.

Figure 7 presents the bias of GOCI high-resolution YAER AOD compared to AERONET AOD. The points of Fig. 7a-c are the median of collocated records sorted in ascending order based on the x axis variable, divided into 19, 18, and 9 intervals for all domains, land, and ocean, respectively. For Fig. 7d, the median values of collocated records for each GOCI observation hour are shown. Land and ocean points are collected by masking out retrieved ocean and land pixels using the land-sea mask in the co-location process, respectively. For all four variables, the bias of GOCI AOD is mostly around -0.05–0.05 range, showing a good agreement to AERONET. When AERONET AOD is larger than 1, GOCI AOD slightly underestimates, with a bias of approximately -0.1 (Fig. 7a). There were some overestimations in GOCI ocean retrievals in the NDVI range of -0.2–-0.1, which is due to AOD overestimation over turbid water. Over land, some overestimation of AOD is observed presented over a low NDVI range (Fig. 7b). The overestimation of AOD over turbid water and sparsely vegetated land indicates that the surface reflectance *a priori* over these regions is underestimated. The diurnal bias of GOCI AOD is minimal, where the lowest and highest bias are within the -0.05–0.05 range. The underestimation of AOD during the morning and late afternoon can be attributed to extended light paths during these hours compared to other hours.

https://doi.org/10.5194/essd-2025-281
Preprint. Discussion started: 30 May 2025

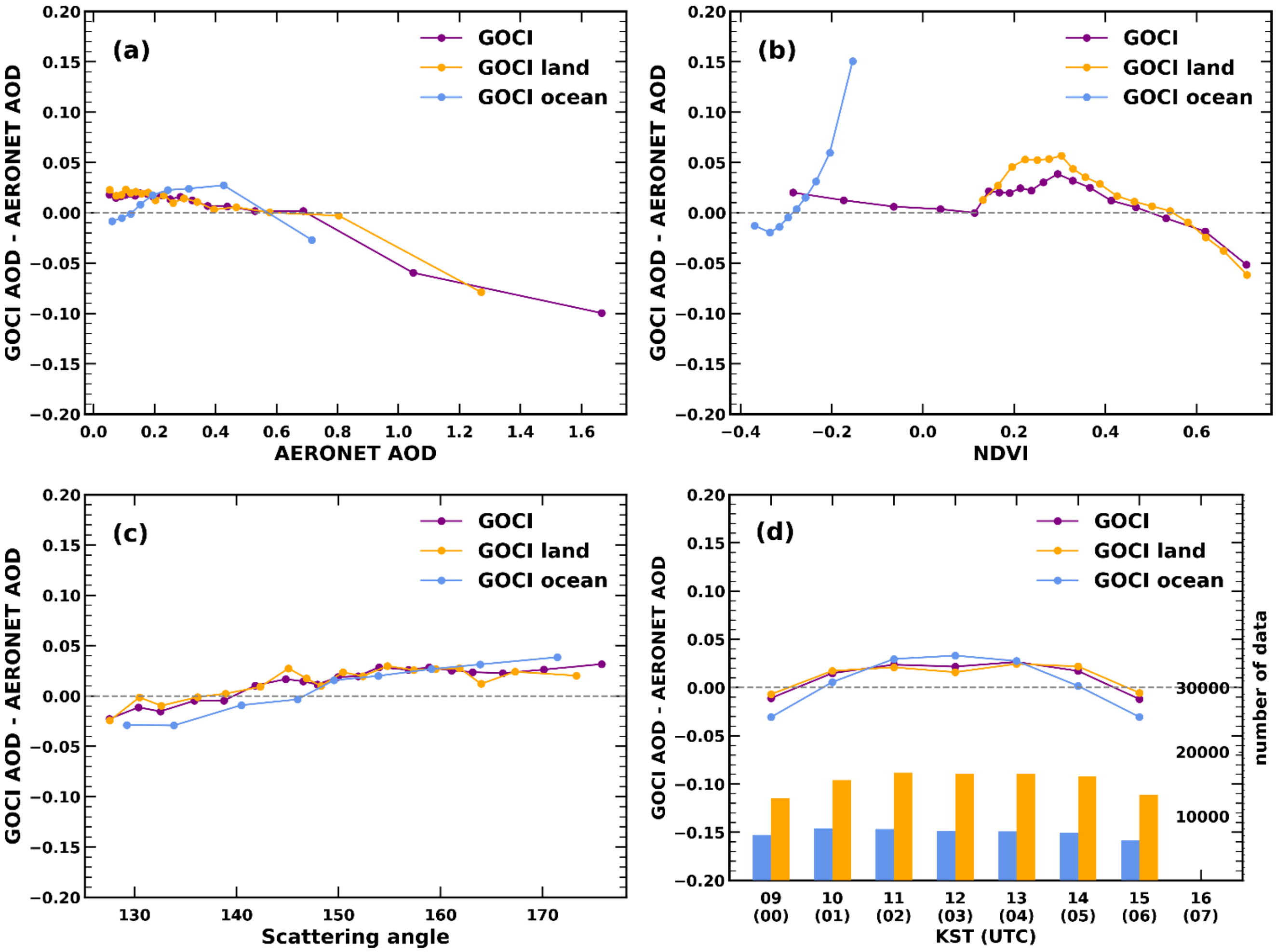

Figure 7. Bias of GOCI high-resolution YAER AOD compared to AERONET, according to (a) AERONET AOD, (b) NDVI, (c) scattering angle, and (d) GOCI observation time. The vertical bars of (d) represent the number of data collocated to AERONET.

3.3 Decadal AOD trend analysis

The GOCI high-resolution YAER AOD dataset provides consistent decadal information over East Asia, during a period in which AOD was declining steeply, and also includes diurnal variation of AOD. Figure 8 shows the average GOCI AOD (Fig. 8a) and the trends of AOD (Fig. 8b) for each product resolution pixel. When calculating averages in Fig. 8a, hourly retrievals were averaged into daily average, and the daily averages of 10 years were averaged to yield Fig. 8a. When calculating trends in Fig. 8b, the trend was calculated by linearly interpolating the yearly average AOD from 2012 to 2020 to remove the effects of monthly variations and seasonality. Note that 2012 and 2020 were used to ensure the robustness because for 2011, the observation began in March, and for 2021, the observation ended in March. The average AOD over East Asia revealed regions where AOD increments stand out compared to surrounding regions; vast regions of Eastern China and most populated and

https://doi.org/10.5194/essd-2025-281
Preprint. Discussion started: 30 May 2025

industrialized cities of South Korea and Japan had a higher AOD than the background. This clearly implies the non-negligible effect of anthropogenic aerosols over East Asia throughout the decade (Hu et al., 2017). Compared to the near-zero AOD of the Pacific Ocean, AOD over the Yellow Sea (between Eastern China and the Korean Peninsula) showed higher values between 0.4–0.6, which can be attributed to the long-range transport of aerosols of Eastern China along the westerlies (Lee et al., 2019; Lee et al., 2021).

For most pixels, the GOCI high-resolution YAER AOD decreased throughout 2012 to 2020 (Fig. 8b). The largest decrease of AOD was identified over Eastern China, especially in the Beijing, Tianjin, Hebei, and Shandong provinces (hereinafter the BTH region and its surroundings). This result aligns with the result of previous studies using LEO satellites and reanalysis during similar time periods (Sogacheva et al., 2018; Sun et al., 2019; Li, 2020). The ΔAOD $year^{-1}$ calculated from earlier studies slightly varies, where our dataset shows about -0.05 ΔAOD $year^{-1}$ over the BTH region and its surroundings, whereas Sogacheva et al. (2018) and Sun et al. (2019) implied approximately -0.07 ΔAOD $year^{-1}$ (for 2011–2017) and -0.03 ΔAOD $year^{-1}$ (for 2010–2017), respectively (see their Fig. 7 and Fig. 11). The minor discrepancies between the studies are due to the difference in the dataset itself, the spatial and temporal resolution of the dataset, and the period used in the analysis.

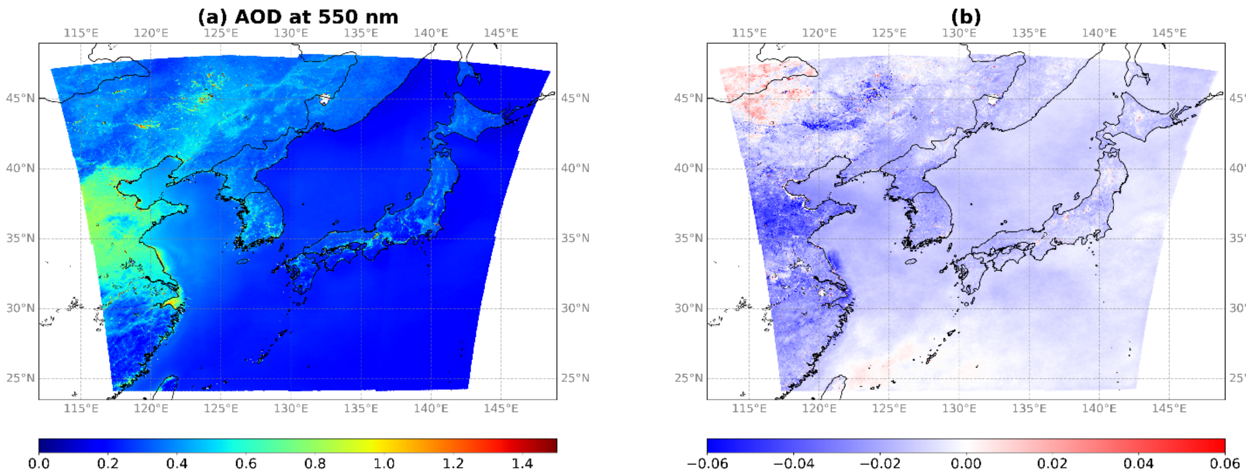

Figure 8. (a) Average GOCI high-resolution YAER AOD during the whole observation period and (b) the trends of AOD (ΔAOD $year^{-1}$) for each pixel. For (b), only the pixels with p-values less than 0.05 are shown in colors.

The trend of AOD for each city is shown with its monthly averages (Fig. 9). As time progresses, AOD displayed a decreasing trend in the order of Beijing, Pyongyang, Seoul, and Tokyo. AOD peaked during summer because the high relative humidity of East Asia during the summer enhances aerosol hygroscopic growth (Fan et al., 2020).

https://doi.org/10.5194/essd-2025-281
Preprint. Discussion started: 30 May 2025

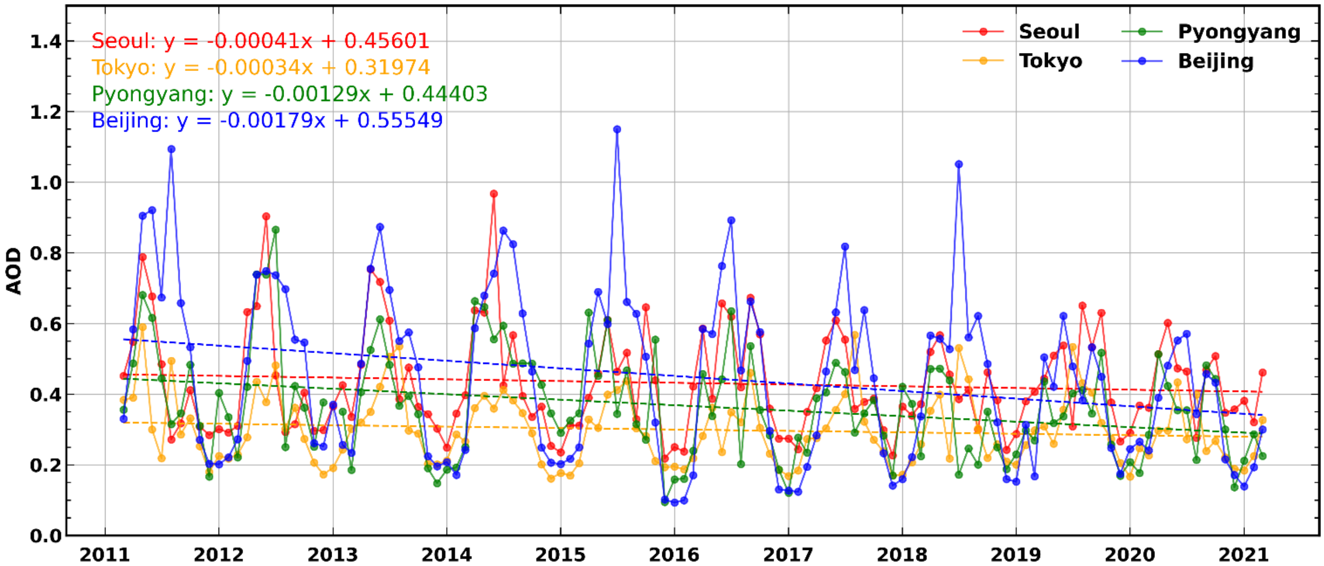

Figure 9. Trends of GOCI high-resolution YAER AOD for Seoul (red), Tokyo (yellow), Pyongyang (green), and Beijing (blue). The grid boxes of each city are marked in Fig 1.

4 Data availability

The GOCI high-resolution YAER aerosol optical properties is saved in NetCDF-4 format and is publicly available at https://doi.org/10.7910/DVN/WWLI4W (Lee et al., 2025). The hourly NetCDF-4 files can be accessed by opening the monthly zipped file. The hourly data ranges from March 1st, 2011, 00:16:42 UTC to March 31st, 2021, 07:16:41 UTC. The ancillary variables, namely longitude, latitude, VZA, the viewing azimuth angle, and the land-sea mask at the product resolution are provided as a separate file, named as "GOCI_YAERAERO_hires_navigation.nc". The whole dataset shares the same coordinates and ancillary variables.

5 Conclusion

The GOCI high-resolution aerosol dataset was designed to meet recent user demands and provide enhanced information on aerosol optical properties over long term. The high-resolution dataset encompasses Northeastern Asia, the region where the characteristics and distribution of aerosols were complex during the GOCI observation period of March 2011 to March 2021. The dataset is provided at one-hour intervals, from 00:30 UTC to 07:30 UTC, which is the daytime in the local area. The hourly dataset includes five properties: the AOD, FMF, SSA, AE, and aerosol type. The high-resolution product has 2 km × 2 km spatial resolution at nadir, which is nine times finer than the 6 km resolution of the operational version. The dataset is available online at https://doi.org/10.7910/DVN/WWLI4W (Lee et al., 2025) in NetCDF-4 format.

https://doi.org/10.5194/essd-2025-281
Preprint. Discussion started: 30 May 2025

The GOCI high-resolution YAER algorithm mainly consists of three steps, namely cloud detection and pixel aggregation, classification of surface regimes, and inversion. Hourly radiances observed from eight channels of GOCI are used as a major input for the retrieval. First, multiple criteria including spectral reflectance, its standard deviations, and thresholds are adopted to screen out unsuitable pixels at the observation resolution for aerosol retrieval, such as cloudy, snowy, and bright surface pixels over both land and ocean. Then, the remaining observation resolution pixels are aggregated into the product resolution. Each pixel is assigned into one of the three regimes: land, ocean, and turbid water. The darkest 1-3% of RCR is regarded as the surface reflectance for land and turbid water, whereas the climatology of wind speed is used to calculate the surface reflectance for the ocean. Inversion is conducted using a pre-calculated LUT, where the AOD is retrieved as a primary product, and the FMF, SSA, AE, and aerosol type are calculated as by-products.

The characteristics of GOCI high-resolution dataset were investigated. Over the ocean where clouds leave clear-sky pixels in between, the high-resolution products show more intricate features around clouds. Around the coastlines of the Korean Peninsula where turbid water and red tides frequently occur, the high-resolution products demonstrate a more refined quality compared to the operational version. While discrete discontinuity occurs in the operational version due to a mixed signal of land and ocean being reflected in a single pixel, the high-resolution pixels provide a more realistic view of the coastal AOD. In addition, a high-AOD event over SMA was analyzed at the pixel level. Compared to 6 km pixels which cover one or two sub-districts, the high-resolution pixels capture variations of AOD within individual sub-district in SMA. The high-resolution products excluded the influence of inland water pixels, which can introduce unexpected biases at coarser resolutions.

The trends and distributions of decadal high-resolution dataset were analyzed from various perspectives. During the 2010s, some East Asian countries tightened their regulations on air pollutant emissions to improve air quality and promote public health. The impact of these regulations was captured by the GOCI high-resolution dataset; although most of the GOCI FOR experienced a significant decrease in AOD, this trend was most pronounced in Eastern China. When averaged monthly, AOD peaked at summertime, reflecting the effect of hygroscopic growth of aerosols during humid East Asian summer.

We validated the GOCI high-resolution aerosol products to AERONET, a ground-truth reference dataset, by collocating the two datasets spatially and temporally. The decadal GOCI high-resolution AOD divided into four seasons showed good agreement to AERONET direct sun products, showing the % within EE as high as 64.5%. The bias of GOCI high-resolution AOD against AERONET AOD was analyzed in terms of AERONET AOD, NDVI, scattering angle, and GOCI observation time. Most AOD bias was constrained within the ±0.05 envelope, except for an overestimation issue over turbid water. Most notably, the retrieval algorithm and the resulting product maintained its performance throughout the observation times, proving its diurnal stability.

The proposed GOCI high-resolution YAER aerosol products are anticipated to be applied in various studies. For example, this data has been utilized in producing a high-resolution $PM_{2.5}$ dataset, providing a more detailed view of surface-level air pollution over East Asia (Pendergrass et al., 2025). With detailed information on clear-sky pixels around clouds, the dataset can be incorporated into aerosol-cloud interaction studies (Myhre et al., 2007; Bai et al., 2020). With its advanced quality along coastlines, the high-resolution products can contribute to a more accurate atmospheric correction over these areas and may assist research on the relationship between AOD and marine microorganisms such as chlorophyll-a (Shen et al., 2020). Furthermore, since the high-resolution dataset has a similar spatial resolution to GOCI-II, an analysis combining GOCI and GOCI-II would reveal an insight into long-term AOD trends and diurnal variations.

Overall, the GOCI high-resolution YAER aerosol products have high spatiotemporal resolution, promising accuracy, and long-term records to reveal valuable information on aerosol characteristics and distribution over East Asia. Further studies using the algorithm may be conducted on recently launched satellites such as GOCI-II to magnify the usage of this state-of-the-art satellite.

Author contribution

JWL and SL performed dataset production, curation and evaluation. JK managed project administration, supervised the project, acquired funding. SL, MC, and JHL designed the methodology and analyzed the data. MC, JHL, DJ, SK, and YP provided guidance and revised the manuscript. YP provided support as project manager throughout the GOCI mission. All authors contributed to authorship, participated in discussions, and provided advice on the manuscript.

Competing interests

The contact author has declared that none of the authors has any competing interests.

Acknowledgements

This material is based on work supported by Samsung Advanced Institute of Technology and National Research Foundation of Korea (NRF) grant funded by the Korea government (MSIT). This work was supported by the Yonsei Fellow Program, funded by Lee Youn Jae. The authors would also like to acknowledge the support by the Korea Institute of Ocean Science and Technology (KIOST) for providing GOCI observations. We thank the PIs and their staff for establishing and maintaining the AERONET sites used for LUT generation and validation of the retrieved properties in this study.

Financial Support

This work was supported by Samsung Advanced Institute of Technology (2021-11-2232). This work was supported by the National Research Foundation of Korea (NRF) grant funded by the Korea government (MSIT) (RS-2024-00346149).

https://doi.org/10.5194/essd-2025-281
Preprint. Discussion started: 30 May 2025

References

Ahn, J.-H., Park, Y.-J., Ryu, J.-H., Lee, B., and Oh, I. S.: Development of atmospheric correction algorithm for Geostationary Ocean Color Imager (GOCI), Ocean Science Journal, 47, 247–259, https://doi.org/10.1007/s12601-012-0026-2, 2012.

Anderson, T. L.: Testing the MODIS satellite retrieval of aerosol fine-mode fraction, Journal of Geophysical Research, 110, https://doi.org/10.1029/2005jd005978, 2005.

Andreae, M. O.: Atmospheric Aerosols: Biogeochemical Sources and Role in Atmospheric Chemistry, Science, 276, 1052–1058, https://doi.org/10.1126/science.276.5315.1052, 1997.

Bai, H., Wang, M., Zhang, Z., and Liu, Y.: Synergetic Satellite Trend Analysis of Aerosol and Warm Cloud Properties ver Ocean and Its Implication for Aerosol-Cloud Interactions, Journal of Geophysical Research: Atmospheres, 125, https://doi.org/10.1029/2019jd031598, 2020.

Baldacci, S., Maio, S., Cerrai, S., Sarno, G., Baïz, N., Simoni, M., Annesi-Maesano, I., and Viegi, G.: Allergy and asthma: Effects of the exposure to particulate matter and biological allergens, Respiratory Medicine, 109, 1089–1104, https://doi.org/10.1016/j.rmed.2015.05.017, 2015.

Bellouin, N., Quaas, J., Gryspeerdt, E., Kinne, S., Stier, P., Watson-Parris, D., Boucher, O., Carslaw, K. S., Christensen, M., Daniau, A. -L., Dufresne, J. -L., Feingold, G., Fiedler, S., Forster, P., Gettelman, A., Haywood, J. M., Lohmann, U., Malavelle, F., Mauritsen, T., and McCoy, D. T.: Bounding Global Aerosol Radiative Forcing of Climate Change, Reviews of Geophysics, 58, https://doi.org/10.1029/2019rg000660, 2020.

Burnett, R., Chen, H., Szyszkowicz, M., Fann, N., Hubbell, B., Pope, C. A., Apte, J. S., Brauer, M., Cohen, A., Weichenthal, S., Coggins, J., Di, Q., Brunekreef, B., Frostad, J., Lim, S. S., Kan, H., Walker, K. D., Thurston, G. D., Hayes, R. B., and Lim, C. C.: Global estimates of mortality associated with long-term exposure to outdoor fine particulate matter, Proceedings of the National Academy of Sciences, 115, 9592–9597, https://doi.org/10.1073/pnas.1803222115, 2018.

Charlson, R. J.: Atmospheric visibility related to aerosol mass concentration: review, Environmental science & technology, 3, 913–918, https://doi.org/10.1021/es60033a002, 1969.

Choi, J.-K., Park, Y. J., Ahn, J. H., Lim, H.-S., Eom, J., and Ryu, J.-H.: GOCI, the world's first geostationary ocean color observation satellite, for the monitoring of temporal variability in coastal water turbidity, Journal of Geophysical Research: Oceans, 117, n/a-n/a, https://doi.org/10.1029/2012jc008046, 2012.

Choi, J.-K., Park, Y. J., Lee, B. R., Eom, J., Moon, J.-E., and Ryu, J.-H.: Application of the Geostationary Ocean Color Imager (GOCI) to mapping the temporal dynamics of coastal water turbidity, Remote Sensing of Environment, 146, 24–35, https://doi.org/10.1016/j.rse.2013.05.032, 2014.

Choi, M. Y., Kim, J., Lee, J.-H., Kim, M., Park, Y.-J., Jeong, U., Kim, W., Hong, H., Holben, B. N., Eck, T. F., Song, C.-K., Lim, J.-H., and Song, C.-K.: GOCI Yonsei Aerosol Retrieval (YAER) algorithm and validation during the DRAGON-NE Asia 2012 campaign, Atmospheric Measurement Techniques, 9, 1377–1398, https://doi.org/10.5194/amt-9-1377-2016, 2016.

Choi, M., Kim, J., Lee, J.-H., Kim, M., Young Je Park, Holben, B. N., Eck, T. F., Li, Z., and Song, C. H.: GOCI Yonsei aerosol retrieval version 2 products: an improved algorithm and error analysis with uncertainty estimation from 5-year validation over East Asia, Atmospheric Measurement Techniques, 11, 385–408, https://doi.org/10.5194/amt-11-385-2018, 2018.

Choi, M. Y., Lim, H., Kim, J., Lee, S., Eck, T. F., Holben, B. N., Garay, M. J., Hyer, E. J., Saide, P. E., and Liu, H.: Validation, comparison, and integration of GOCI, AHI, MODIS, MISR, and VIIRS aerosol optical depth over East Asia during the 2016 KORUS-AQ campaign, Atmospheric Measurement Techniques, 12, 4619–4641, https://doi.org/10.5194/amt-12-4619-2019, 2019.

Cox, C. S. and Munk, W.: Measurement of the Roughness of the Sea Surface from Photographs of the Sun's Glitter, Journal of the Optical Society of America, 44, 838–838, https://doi.org/10.1364/josa.44.000838, 1954.

Crawford, J. H., Ahn, J.-Y., Al-Saadi, J., Chang, L., Emmons, L. K., Kim, J., Lee, G., Park, J.-H., Park, R. J., Woo, J. H., Song, C.-K., Hong, J.-H., Hong, Y.-D., Lefer, B. L., Lee, M., Lee, T., Kim, S., Min, K.-E., Yum, S. S., and Shin, H. J.: The Korea–United States Air Quality (KORUS-AQ) field study, Elementa: Science of the Anthropocene, 9, https://doi.org/10.1525/elementa.2020.00163, 2021.

Dockery, D. W., Schwartz, J., and Spengler, J. D.: Air pollution and daily mortality: Associations with particulates and acid aerosols, Environmental Research, 59, 362–373, https://doi.org/10.1016/s0013-9351(05)80042-8, 1992.

Eck, T. F., Holben, B. N., Reid, J. S., Dubovik, O., Smirnov, A., O'Neill, N. T., Slutsker, I., and Kinne, S.: Wavelength dependence of the optical depth of biomass burning, urban, and desert dust aerosols, Journal of Geophysical Research: Atmospheres, 104, 31333–31349, https://doi.org/10.1029/1999jd900923, 1999.

Eck, T. F., Holben, B. N., Kim, J., Beyersdorf, A. J., Choi, M., Lee, S., Koo, J.-H., Giles, D. M., Schafer, J. S., Sinyuk, A., Peterson, D. A., Reid, J. S., Arola, A., Slutsker, I., Smirnov, A., Sorokin, M., Kraft, J., Crawford, J. H., Anderson, B. E., and Thornhill, K. L.: Influence of cloud, fog, and high relative humidity during pollution transport events in South Korea: Aerosol properties and PM2.5 variability, Atmospheric Environment, 232, 117530–117530, https://doi.org/10.1016/j.atmosenv.2020.117530, 2020.

Fan, M., He, G., and Zhou, M.: The winter choke: Coal-Fired heating, air pollution, and mortality in China, Journal of Health Economics, 71, 102316, https://doi.org/10.1016/j.jhealeco.2020.102316, 2020.

Giles, D. M., Sinyuk, A., Sorokin, M. G., Schafer, J. S., Smirnov, A., Slutsker, I., Eck, T. F., Holben, B. N., Lewis, J. R., Campbell, J. R., Welton, E. J., Korkin, S. V., and Lyapustin, A. I.: Advancements in the Aerosol Robotic Network (AERONET) Version 3 database – automated near-real-time quality control algorithm with improved cloud screening for Sun photometer aerosol optical depth (AOD) measurements, Atmospheric Measurement Techniques, 12, 169–209, https://doi.org/10.5194/amt-12-169-2019, 2019.

Han, C., Lim, Y.-H., Yorifuji, T., and Hong, Y.-C.: Air quality management policy and reduced mortality rates in Seoul Metropolitan Area: A quasi-experimental study, Environment International, 121, 600–609, https://doi.org/10.1016/j.envint.2018.09.047, 2018.

https://doi.org/10.5194/essd-2025-281
Preprint. Discussion started: 30 May 2025

Holben, B. N., Eck, T. F., Slutsker, I., Tanré, D., Buis, J. P., Setzer, A., Vermote, E., Reagan, J. A., Kaufman, Y. J., Nakajima, T., Lavenu, F., Jankowiak, I., and Smirnov, A.: AERONET—A Federated Instrument Network and Data Archive for Aerosol Characterization, Remote Sensing of Environment, 66, 1–16, https://doi.org/10.1016/s0034-4257(98)00031-5, 1998.

Holben, B. N., Kim, J., Sano, I., Mukai, S., Eck, T. F., Giles, D. M., Schafer, J. S., Sinyuk, A., Slutsker, I., Smirnov, A., Sorokin, M., Anderson, B. E., Che, H., Choi, M., Crawford, J. H., Ferrare, R. A., Garay, M. J., Jeong, U., Kim, M., and Kim, W.: An overview of mesoscale aerosol processes, comparisons, and validation studies from DRAGON networks, Atmospheric Chemistry and Physics, 18, 655–671, https://doi.org/10.5194/acp-18-655-2018, 2017.

Hsu, N. C., Tsay, S.-C. ., King, M. D., and Herman, J. R.: Aerosol Properties Over Bright-Reflecting Source Regions, IEEE Transactions on Geoscience and Remote Sensing, 42, 557–569, https://doi.org/10.1109/tgrs.2004.824067, 2004.

Hsu, N. C., Jeong, M.-J. ., Bettenhausen, C., Sayer, A. M., Hansell, R., Seftor, C. S., Huang, J., and Tsay, S.-C. .: Enhanced Deep Blue aerosol retrieval algorithm: The second generation, Journal of Geophysical Research: Atmospheres, 118, 9296–9315, https://doi.org/10.1002/jgrd.50712, 2013.

Hsu, N. C., Lee, J., Sayer, A. M., Kim, W., Bettenhausen, C., and Tsay, S. -C.: VIIRS Deep Blue Aerosol Products Over Land: Extending the EOS Long-Term Aerosol Data Records, Journal of Geophysical Research: Atmospheres, 124, 4026–4053, https://doi.org/10.1029/2018jd029688, 2019.

Hu, J. F., Wang, P., Ying, Q., Zhang, H. Y., Chen, J., Ge, X., Li, X., Jiang, J., Wang, S.-M., Zhang, J., Zhao, Y., and Zhang, Y.-Y.: Modeling biogenic and anthropogenic secondary organic aerosol in China, Atmospheric Chemistry and Physics, 17, 77–92, https://doi.org/10.5194/acp-17-77-2017, 2016.

IOCCG: Ocean-colour Observations from a Geostationary Orbit. IOCCG, Dartmouth, Canada, 2012.

Kaufman, Y. J., Tanré, D., and Boucher, O.: A satellite view of aerosols in the climate system, Nature, 419, 215–223, https://doi.org/10.1038/nature01091, 2002.

Kim, M., Kim, J., Jeong, U., Kim, W., Hong, H., Holben, B., Eck, T. F., Lim, J. H., Song, C. K., Lee, S., and Chung, C.-Y.: Aerosol optical properties derived from the DRAGON-NE Asia campaign, and implications for a single-channel algorithm to retrieve aerosol optical depth in spring from Meteorological Imager (MI) on-board the Communication, Ocean, and Meteorological Satellite (COMS), Atmospheric chemistry and physics, 16, 1789–1808, https://doi.org/10.5194/acp-16-1789-2016, 2016.

Kim, W., Moon, J.-E., Park, Y.-J., and Ishizaka, J.: Evaluation of chlorophyll retrievals from Geostationary Ocean Color Imager (GOCI) for the North-East Asian region, Remote Sensing of Environment, 184, 482–495, https://doi.org/10.1016/j.rse.2016.07.031, 2016.

Kim, J., Jeong, U., Ahn, M.-H., Kim, J. H., Park, R. J., Lee, H., Song, C. H., Choi, Y.-S., Lee, K.-H., Yoo, J.-M., Jeong, M.-J., Park, S. K., Lee, K.-M., Song, C.-K., Kim, S.-W., Kim, Y. J., Kim, S.-W., Kim, M., Go, S., and Liu, X.: New Era of Air Quality Monitoring from Space: Geostationary Environment Monitoring Spectrometer (GEMS), Bulletin of the American Meteorological Society, 101, E1–E22, https://doi.org/10.1175/bams-d-18-0013.1, 2020.

https://doi.org/10.5194/essd-2025-281
Preprint. Discussion started: 30 May 2025

Kim, M., Kim, J., Lim, H., Lee, S., Cho, Y., Lee, Y.-G., Go, S., and Lee, K.: Aerosol optical depth data fusion with Geostationary Korea Multi-Purpose Satellite (GEO-KOMPSAT-2) instruments GEMS, AMI, and GOCI-II: statistical and deep neural network methods, Atmospheric Measurement Techniques, 17, 4317–4335, https://doi.org/10.5194/amt-17-4317-2024, 2024.

Koelemeijer, R. B. A., de Haan, J. F., and Stammes, P.: A database of spectral surface reflectivity in the range 335–772 nm derived from 5.5 years of GOME observations, Journal of Geophysical Research, 108, https://doi.org/10.1029/2002jd002429, 2003.

Lee, J., Kim, J., Song, C.-K., Ryu, J.-H., Ahn, Y.-H., and Song, C.: Algorithm for retrieval of aerosol optical properties over the ocean from the Geostationary Ocean Color Imager, Remote Sensing of Environment, 114, 1077–1088, https://doi.org/10.1016/j.rse.2009.12.021, 2010a.

Lee, J., Kim, J., Song, C. H., Kim, S. B., Chun, Y., Sohn, B. J., and Holben, B. N.: Characteristics of aerosol types from AERONET sunphotometer measurements, Atmospheric Environment, 44, 3110–3117, https://doi.org/10.1016/j.atmosenv.2010.05.035, 2010b.

Lee, S., Kim, J., Choi, M., Hong, J., Lim, H., Eck, T. F., Holben, B. N., Ahn, J.-Y., Kim, J., and Koo, J.-H.: Analysis of long-range transboundary transport (LRTT) effect on Korean aerosol pollution during the KORUS-AQ campaign, Atmospheric Environment, 204, 53–67, https://doi.org/10.1016/j.atmosenv.2019.02.020, 2019.

Lee, M.-S., Park, K.-A., and Micheli, F.: Derivation of Red Tide Index and Density Using Geostationary Ocean Color Imager (GOCI) Data, Remote Sensing, 13, 298, https://doi.org/10.3390/rs13020298, 2021.

Lee, S., Kim, M., Kim, S.-Y., Dong Ho Lee, Lee, H., Kim, J., Le, S., and Liu, Y.: Assessment of long-range transboundary aerosols in Seoul, South Korea from Geostationary Ocean Color Imager (GOCI) and ground-based observations, Environmental Pollution, 269, 115924–115924, https://doi.org/10.1016/j.envpol.2020.115924, 2021.Lee, S., Choi, M., Kim, J., Park, Y.-J., Choi, J.-K., Lim, H., Lee, J., Kim, M., and Cho, Y.: Retrieval of aerosol optical properties from GOCI-II observations: Continuation of long-term geostationary aerosol monitoring over East Asia, The Science of The Total Environment, 903, 166504–166504, https://doi.org/10.1016/j.scitotenv.2023.166504, 2023.Lee, J., Cho, Y., Lee, S., Kim, J., and Park, Y.-J.: Near-real-time hourly PM2.5 prediction over East Asia using geostationary satellite products and machine learning, Atmospheric Environment, 334, 120700, https://doi.org/10.1016/j.atmosenv.2024.120700, 2024.

Lee, J., Hsu, N. C., Kim, W. V., Sayer, A. M., and Tsay, S.: VIIRS Version 2 Deep Blue Aerosol Products, Journal of Geophysical Research: Atmospheres, 129, https://doi.org/10.1029/2023jd040082, 2024.

Lee, J., Kim, J., Lee, S., Choi, M., Lee, J., Jacob, D. J., Kuk, S. K., Park, and Y.-J.: A decadal, hourly high-resolution GOCI aerosol optical properties over East Asia, Harvard Dataverse [data set], https://doi.org/10.7910/DVN/WWLI4W

Lennartson, E. M., Wang, J., Gu, J., Garcia, L., Ge, C., Gao, M., Choi, M. Y., Saide, P. E., Carmichael, G. R., Kim, J., and Janz, S. J.: Diurnal variation of aerosol optical depth and PM_{2.5} in South Korea: a synthesis from AERONET, satellite (GOCI), KORUS-AQ observation, and the WRF-Chem model, Atmospheric Chemistry and Physics, 18, 15125–15144, https://doi.org/10.5194/acp-18-15125-2018, 2018.

https://doi.org/10.5194/essd-2025-281
Preprint. Discussion started: 30 May 2025

Levy, R. C., Remer, L. A., Kleidman, R. G., Mattoo, S., Ichoku, C., Kahn, R., and Eck, T. F.: Global evaluation of the Collection 5 MODIS dark-target aerosol products over land, Atmospheric Chemistry and Physics, 10, 10399–10420, https://doi.org/10.5194/acp-10-10399-2010, 2010.

Levy, R. C., Mattoo, S., Munchak, L. A., Remer, L. A., Sayer, A. M., Patadia, F., and Hsu, N. C.: The Collection 6 MODIS aerosol products over land and ocean, Atmospheric Measurement Techniques, 6, 2989–3034, https://doi.org/10.5194/amt-6-2989-2013, 2013.

Li, R.-R., Kaufman, Y. J., Gao, B.-C., and Davis, C. O.: Remote sensing of suspended sediments and shallow coastal waters, IEEE Transactions on Geoscience and Remote Sensing, 41, 559–566, https://doi.org/10.1109/tgrs.2003.810227, 2003.

Li, J.: Pollution Trends in China from 2000 to 2017: A Multi-Sensor View from Space, Remote Sensing, 12, 208, https://doi.org/10.3390/rs12020208, 2020.

Lim, H., Go, S., Kim, J., Choi, M., Lee, S., Song, C.-K., and Kasai, Y.: Integration of GOCI and AHI Yonsei aerosol optical depth products during the 2016 KORUS-AQ and 2018 EMeRGe campaigns, Atmospheric measurement techniques, 14, 4575–4592, https://doi.org/10.5194/amt-14-4575-2021, 2021.

Lyapustin, A., Wang, Y., Korkin, S., and Huang, D.: MODIS Collection 6 MAIAC algorithm, Atmospheric Measurement Techniques, 11, 5741–5765, https://doi.org/10.5194/amt-11-5741-2018, 2018.

Lyapustin, A., Wang, Y., Choi, M., Xiong, X., Angal, A., Wu, A., Doelling, D. R., Bhatt, R., Go, S., Korkin, S., Franz, B., Meister, G., Sayer, A. M., Roman, M., Holz, R. E., Meyer, K., Gleason, J., and Levy, R.: Calibration of the SNPP and NOAA 20 VIIRS sensors for continuity of the MODIS climate data records, Remote Sensing of Environment, 295, 113717–113717, https://doi.org/10.1016/j.rse.2023.113717, 2023.

Mayer, B. and Kylling, A.: Technical note: The libRadtran software package for radiative transfer calculations - description and examples of use, Atmospheric Chemistry and Physics, 5, 1855–1877, https://doi.org/10.5194/acp-5-1855-2005, 2005.

Myhre, G., Frode Stordal, Johnsrud, M., Kaufman, Y., Rosenfeld, D., Trude Storelvmo, Jon Egill Kristjansson, Terje Koren Berntsen, Myhre, A., and Isaksen, I. S. A.: Aerosol-cloud interaction inferred from MODIS satellite data and global aerosol models, Atmospheric Chemistry and Physics, 7, 3081–3101, https://doi.org/10.5194/acp-7-3081-2007, 2007.

Pang, J., Liu, Z., Wang, X., Bresch, J. F., Ban, J., Chen, D., and Kim, J.: Assimilating AOD retrievals from GOCI and VIIRS to forecast surface PM2.5 episodes over Eastern China, Atmospheric Environment, 179, 288–304, https://doi.org/10.1016/j.atmosenv.2018.02.011, 2018.

Pendergrass, D. C., Jacob, D. J., Oak, Y. J., Lee, J., Kim, M., Kim, J., Lee, S., Zhai, S., Irie, H., and Liao, H.: A continuous 2011–2022 record of fine particulate matter (PM2.5) in East Asia at daily 2-km resolution from geostationary satellite observations: Population exposure and long-term trends, Atmospheric Environment, 346, 121068, https://doi.org/10.1016/j.atmosenv.2025.121068, 2025.

Pu, Q. and Yoo, E.-H.: A gap-filling hybrid approach for hourly PM2.5 prediction at high spatial resolution from multi-sourced AOD data, Environmental Pollution, 315, 120419–120419, https://doi.org/10.1016/j.envpol.2022.120419, 2022.

https://doi.org/10.5194/essd-2025-281
Preprint. Discussion started: 30 May 2025

Open Access Earth System Science Data Discussions

Pye, H. O. T., Ward-Caviness, C. K., Murphy, B. N., Appel, K. W., and Seltzer, K. M.: Secondary organic aerosol association with cardiorespiratory disease mortality in the United States, Nature Communications, 12, https://doi.org/10.1038/s41467-021-27484-1, 2021.

Ryu, J.-H., Han, H.-J., Cho, S., Park, Y.-J., and Ahn, Y.-H.: Overview of geostationary ocean color imager (GOCI) and GOCI data processing system (GDPS), Ocean Science Journal, 47, 223–233, https://doi.org/10.1007/s12601-012-0024-4, 2012.

Saide, P. E., Kim, J., Song, C. H., Choi, M., Cheng, Y., and Carmichael, G. R.: Assimilation of next generation geostationary aerosol optical depth retrievals to improve air quality simulations, Geophysical Research Letters, 41, 9188–9196, https://doi.org/10.1002/2014gl062089, 2014.

Sawyer, V., Levy, R. C., Mattoo, S., Cureton, G., Shi, Y., and Remer, L. A.: Continuing the MODIS Dark Target Aerosol Time Series with VIIRS, Remote Sensing, 12, 308–308, https://doi.org/10.3390/rs12020308, 2020.

Sayer, A. M., Hsu, N. C., Lee, J., Kim, W. V., and Dutcher, S. T.: Validation, Stability, and Consistency of MODIS Collection 6.1 and VIIRS Version 1 Deep Blue Aerosol Data Over Land, Journal of Geophysical Research: Atmospheres, 124, 4658–4688, https://doi.org/10.1029/2018jd029598, 2019.

Shen, C., Zhao, H., Chen, F., and Xiao, H.: The Distribution of Aerosols and Their Impacts on Chlorophyll-*a* Distribution in the South China Sea, Journal of geophysical research. Biogeosciences, 125, https://doi.org/10.1029/2019jg005490, 2020.

Shi, X. and Brasseur, G. P.: The Response in Air Quality to the Reduction of Chinese Economic Activities during the COVID-19 Outbreak, Geophysical Research Letters, 47, https://doi.org/10.1029/2020gl088070, 2020.

Sinyuk, A., Holben, B. N., Eck, T. F., Giles, D. M., Slutsker, I., Korkin, S., Schafer, J. S., Smirnov, A., Sorokin, M., and Lyapustin, A.: The AERONET Version 3 aerosol retrieval algorithm, associated uncertainties and comparisons to Version 2, Atmospheric Measurement Techniques, 13, 3375–3411, https://doi.org/10.5194/amt-13-3375-2020, 2020.

Sogacheva, L., Rodriguez, E., Kolmonen, P., Virtanen, T. H., Saponaro, G., de Leeuw, G., Georgoulias, A. K., Alexandri, G., Kourtidis, K., and van der A, R. J.: Spatial and seasonal variations of aerosols over China from two decades of multi-satellite observations – Part 2: AOD time series for 1995–2017 combined from ATSR ADV and MODIS C6.1 and AOD tendency estimations, Atmospheric Chemistry and Physics, 18, 16631–16652, https://doi.org/10.5194/acp-18-16631-2018, 2018.

Sun, E., Xu, X., Che, H., Tang, Z., Gui, K., An, L., Lu, C., and Shi, G.: Variation in MERRA-2 aerosol optical depth and absorption aerosol optical depth over China from 1980 to 2017, Journal of Atmospheric and Solar-Terrestrial Physics, 186, 8–19, https://doi.org/10.1016/j.jastp.2019.01.019, 2019.

Wang, Y., Xiong, L., and Tang, M.: Toxicity of inhaled particulate matter on the central nervous system: neuroinflammation, neuropsychological effects and neurodegenerative disease, Journal of Applied Toxicology, 37, 644–667, https://doi.org/10.1002/jat.3451, 2017.

Xu, J.-W., Martin, R. V., A. van Donkelaar, Kim, J., Choi, M., Zhang, Q., Geng, G., Liu, Y., Ma, Z., Huang, L., Wang, Y., Chen, H., Che, H., Lin, P., and Lin, N.: Estimating ground-level PM_{2.5} in eastern China using aerosol optical depth determined from the GOCI satellite instrument, Atmospheric chemistry and physics, 15, 13133–13144, https://doi.org/10.5194/acp-15-13133-2015, 2015.

https://doi.org/10.5194/essd-2025-281
Preprint. Discussion started: 30 May 2025

Zhai, S., Jacob, D. J., Brewer, J. F., Li, K., Moch, J. M., Kim, J., Lee, S., Lim, H., Lee, H. C., Kuk, S. K., Park, R. J., Jeong, J. I., Wang, X., Liu, P., Luo, G., Yu, F., Meng, J., Martin, R. V., Travis, K. R., and Hair, J. W.: Relating geostationary satellite measurements of aerosol optical depth (AOD) over East Asia to fine particulate matter (PM_{2.5}): insights from the KORUS-AQ aircraft campaign and GEOS-Chem model simulations, Atmospheric chemistry and physics, 21, 16775–16791, https://doi.org/10.5194/acp-21-16775-2021, 2021.

Zheng, B., Tong, D., Li, M., Liu, F., Hong, C., Geng, G., Li, H., Li, X., Peng, L., Qi, J., Yan, L., Zhang, Y., Zhao, H., Zheng, Y., He, K., and Zhang, Q.: Trends in China's anthropogenic emissions since 2010 as the consequence of clean air actions, Atmospheric Chemistry and Physics, 18, 14095–14111, https://doi.org/10.5194/acp-18-14095-2018, 2018.

Zheng, B., Zhang, Q., Geng, G., Chen, C., Shi, Q., Cui, M., Lei, Y., and He, K.: Changes in China's anthropogenic emissions and air quality during the COVID-19 pandemic in 2020, Earth System Science Data, 13, 2895–2907, https://doi.org/10.5194/essd-13-2895-2021, 2021.

https://doi.org/10.5194/essd-2025-281
Preprint. Discussion started: 30 May 2025

Appendix A

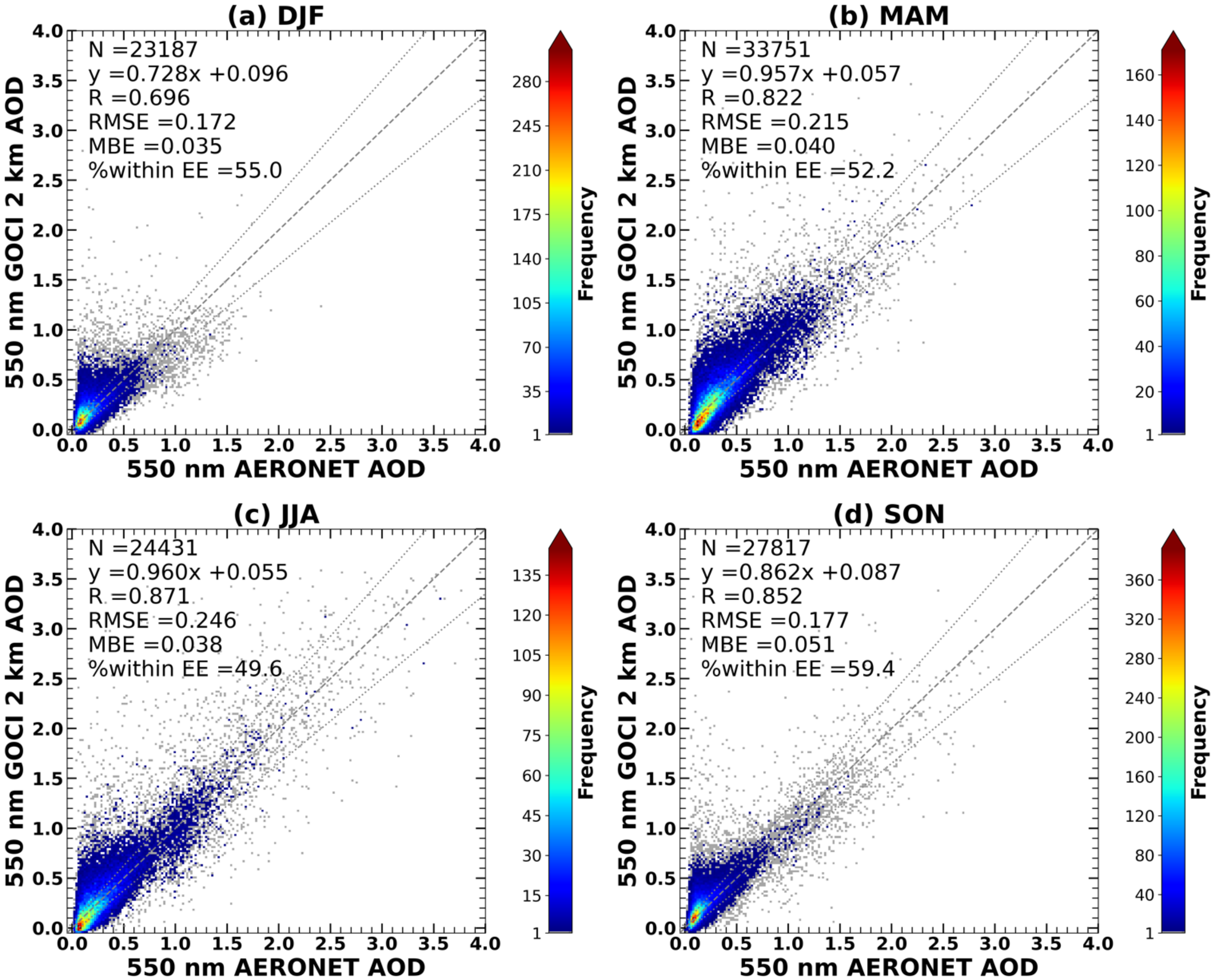

Figure A1. Same as Fig. 5, but for land pixels.

https://doi.org/10.5194/essd-2025-281
Preprint. Discussion started: 30 May 2025

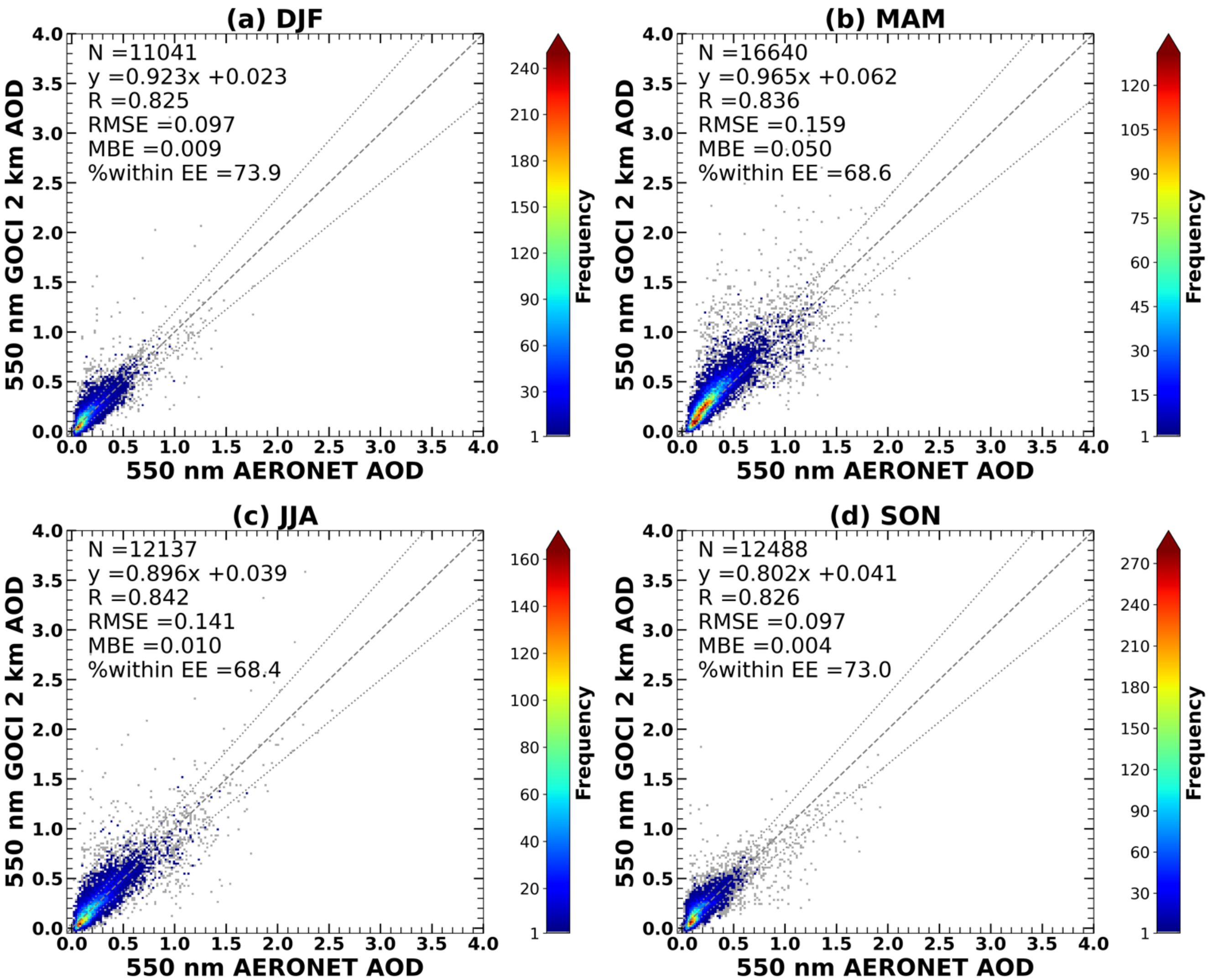

615 **Figure A2. Same as Fig. 5, but for ocean pixels.**